Robust design of polyrhythmic neural circuits

Justus T. C. Schwabedal,[1,][*] Alexander B. Neiman,[2] and Andrey L. Shilnikov[1,3]

[1]*Neuroscience Institute, Georgia State University, Atlanta, Georgia 30303, USA*

[2]*Department of Physics and Astronomy, Ohio University, Athens, Ohio 45701, USA*

[3]*Department of Computational Mathematics and Cybernetics, Lobachevsky State University of Nizhni Novgorod,*
Nizhni Novgorod 603950, Russia

Neural circuit motifs producing coexistent rhythmic patterns are treated as building blocks of multi-functional neuronal networks. We study the robustness of such a motif of inhibitory model neurons to reliably sustain bursting polyrhythms under random perturbations. Without noise, the exponential stability of each of the coexisting rhythms increases with strengthened synaptic coupling, thus indicating an increased robustness. Conversely, after adding noise we find that noise-induced rhythm switching intensifies if the coupling strength is increased beyond a critical value, indicating a decreased robustness. We analyze this stochastic arrhythmia and develop a generic description of its dynamic mechanism. Based on our mechanistic insight, we show how physiological parameters of neuronal dynamics and network coupling can be balanced to enhance rhythm robustness against noise. Our findings are applicable to a broad class of relaxation-oscillator networks, including Fitzhugh-Nagumo and other Hodgkin-Huxley-type networks.

PACS number(s): 87.18.Sn, 05.45.Xt, 87.10.Mn, 87.18.Tt

I. INTRODUCTION

Robustness and flexibility are critical features of physical, social, and biological networks exposed to perturbations in their environment [1–5]. Mechanisms that ensure robust network dynamics can be intricate, especially in genetic [6,7], and neuronal [8–10] networks, for which a high degree of flexibility, i.e., multistability and plasticity, is equally required for proper functioning.

We follow the point of view that functional flexibility in neuronal networks is expressed by the coexistence of multiple dynamical activity patterns, i.e., polyrhythmicity. Each pattern controls a particular function, e.g., coordinated motion [11], sensory perception [12], or memory [13]. These activity patterns are network states of synchronization, notoriously showing a high degree of multiplicity and clustering [14–17]. Perturbations, such as neuronal noise, can destroy such mul-tifunctionality by accidentally switching between coexistent functional patterns [17] and by reducing neuronal synchrony, assumed to be a binding element of neuronal information transmission [18,19]. The interplay between robustness and flexibility was studied in neuronal network models of memory, where an increasing number of stable states, representing individual stored memories, negatively affect the robustness of memory retrieval, thereby leading to false memory associations [20–22].

On a circuitry level, activity patterns are generated by small groups of neurons that are often synaptically coupled to form functional motifs [23–29]. Such neural circuit motifs (NCMs) "are ubiquitous and may serve as computational elements within neural circuits" (Ref. [30], p. 693), including central pattern generators, which produce various motor behaviors autonomously, e.g., heartbeat, respiration, chewing, and locomotion.

Neurons within an NCM often exhibit bursting discharges, i.e., alternation of spike trains and quiescent recovery periods [31,32]. The complex properties of such single-cell activity determine the rhythmic patterns that an NCM can generate autonomously. The pattern repertoire of the NCM also depends on the functional form and strength of synaptic coupling. Inhibitory synaptic coupling facilitates polyrhythmicity in NCMs by actively breaking the globally synchronized state into many coexistent ones. Each of these is characterized by specific phase relationships between bursts [33]. Such polyrhythmicity can already emerge in a network of two bursters [34,35].

Prediction and control of NCM dynamics are bounded by the multiple time scales inherent to bursting, because such dynamics limits the use of conventional analysis methods. Phase reduction, for example, is not applicable in the analysis of stability of burster networks that are strongly coupled. Conversely, random perturbations can effectively elucidate the dynamical stability of such systems that otherwise evade standard analysis methods [36]. Such systems also include those near bifurcations and those that are singularly perturbed [37,38].

In this article, we study the robustness of polyrhythmicity against random perturbations in an NCM model of three mutually inhibiting Hodgkin-Huxley-type bursters. We report a generic mechanism of noise-induced switching between the coexistent bursting patterns. In search of a robust network design, we devise mechanism-based strategies to enhance rhythm robustness while preserving polyrhythmicity.

In the next section, we introduce the NCM model. In Monte Carlo simulations, we identify the noise-induced rhythm switching phenomenon (Sec. III), which we then explain in Sec. IV, using a soft- to hard-lock transition of network dynamics. In Sec. V, we use this mechanistic insight to improve the stability of NCM polyrhythmicity. We end in Sec. VI with concluding remarks.

---

[*]JSchwabedal@gmail.com

II. CIRCUIT MOTIF OF THREE INHIBITORY BURSTING NEURONS

Our NCM consists of three bursting model neurons with reciprocal inhibitory synapses. The NCM shows three stable rhythms with fixed phase relationships between bursts. The stability and robustness of polyrhythms depend on the system and coupling parameters introduced in this section. Complete equations and a list of all parameter values are presented in the Appendix.

A. Single-cell dynamics

Membrane voltages V_i of the NCM neurons follow Hodgkin-Huxley-type dynamics coupled via inhibitory chemical synapses ($i,j = 1,2,3$):

$$C\dot{V}_i = -I_i^{\text{Na}} - I_i^{\text{K}_2} - I_i^{\text{L}} - I_i^{\text{rand}} - \sum_{j \neq i} I_{ij}^{\text{inh}}. \quad (1)$$

Each neuron has a number of intrinsic currents: a sodium-ion current I_i^{Na}, a potassium-ion current $I_i^{\text{K}_2}$, a leak current I_i^{L}, and a random current I_i^{rand}:

$$I_i^{\text{L}} = g_L(V_i - E_{\text{L}}), \quad I_i^{\text{K}_2} = g_{\text{K}_2} m_i^2 (V_i - E_{\text{K}_2}),$$
$$I_i^{\text{Na}} = g_{\text{Na}} m_i^3 h_i (V_i - E_{\text{Na}}), \quad I_i^{\text{rand}} = I_0 + \sigma \xi_i(t). \quad (2)$$

The random current I_i^{rand} is uncorrelated Gaussian white noise with mean I_0 and amplitude σ. We temporarily set $\sigma = 0$ until Sec. II D, to outline the deterministic dynamics.

The Na$^+$ current activates instantaneously, reflected in the immediate change of the gating variable $m_{\text{Na}} = m_{\text{Na}}^\infty(V_i)$. Na$^+$ inactivation h_i and K$^+$ activation m_i, on the other hand, are dynamic:

$$\tau_{\text{Na}} \dot{h}_i = h^\infty(V_i) - h_i, \quad \tau_{\text{K}_2} \dot{m}_i = m_{\text{K}_2}^\infty(V_i) - m_i,$$
$$h^\infty(V) = [1 + \exp(-s^h(V - V^h))]^{-1}, \quad (3)$$
$$m_{\text{K}_2}^\infty(V) = [1 + \exp(-s^{\text{K}_2}(V - V^{\text{K}_2}))]^{-1}.$$

Bursting emerges from the time-scale separation between the fast Na$^+$ inactivation ($\tau_{\text{Na}} = 0.0405$ s) and the slow K$^+$ activation ($\tau_{\text{K}_2} = 0.9$ s): fast spiking of the membrane voltage and Na$^+$ current is interrupted by quiescent states governed by slow modulation of the K$^+$ current (bursting orbit in Fig. 1).

Dynamics of the single-neuron model, including the genesis of bursting patterns, was studied in detail in Refs. [36] and [39–41].

B. Network dynamics

Neurons are networked with inhibitory chemical synapses: the presynaptic neuron j activates its synapses if V_j exceeds the synaptic threshold $\Theta = -40$ mV. An active synapse, in turn, activates the inhibitory current I_{ij}^{inh} of the postsynaptic neuron i [cf. Eq. (1)]. Synapses are inhibitory because they activate channels of ions with a reversal potential, $E_{\text{inh}} = -62.5$ mV, below typical values for the membrane voltage V_i, e.g., chloride channels. Synaptic dynamics is governed by

$$\tau \dot{I}_{ij}^{\text{inh}} = I_{ij}^\infty - I_{ij}^{\text{inh}},$$
$$I_{ij}^\infty = g_{\text{inh}}(V_i - E_{\text{inh}})/[1 + \exp(\lambda(\Theta - V_j))]. \quad (4)$$
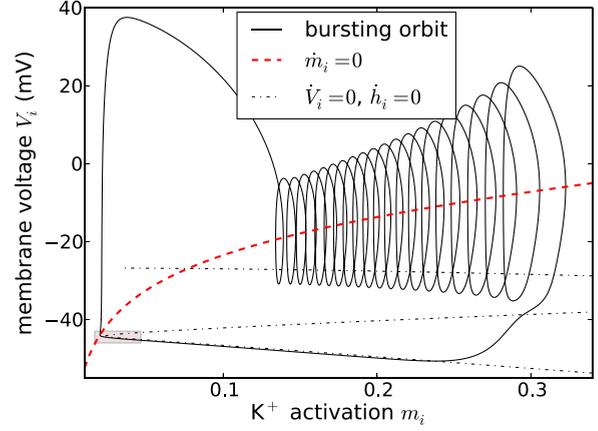
FIG. 1. (Color online) Bursting in the slow-fast Hodgkin-Huxley neuronal model. The bursting orbit of a single neuronal burster (at $\sigma = 0$ and $g_{\text{inh}} = 0$) is organized according to the backbone of nullclines for the slow variable, given by $\dot{m}_i = 0$ [dashed (red) line], and fast variables ($\dot{V}_i, \dot{h}_i) = 0$ (dashed-dotted black lines). The shaded rectangle (lower-left corner) is expanded in Fig. 3.

These synapses are essentially in two states, either active or inactive, as dictated by the activation parameter $\lambda = 1$ mV^{-1}. The conductance g_{inh} parameterizes the synaptic coupling strength. Except in Sec. V B, we investigate instantaneous synapses for which we set $\tau = 0$. At this value of τ, synapses follow the fast threshold modulation framework [40,42,43].

The NCM network dynamics shows coexistent bursting patterns characterized by specific phase relationships: in three *pacemaker patterns* (A, B, and C), one neuron bursts in antiphase with the other two that are in phase (cf. Fig. 2), and two *traveling-wave* patterns consist of three consecutive bursts [43]. Traveling waves dephase immediately under perturbations and are, therefore, not observed. Uniform all-to-all coupling ensures that the remaining three pacemaker patterns are equally stable.

The exponential stability of bursting patterns increases with the coupling strength g_{inh}. Strong coupling, studied in this article, results in very high convergence rates as noticeable by the short transients after pulses in Fig. 2.

C. Soft- to hard-lock transition

Strong synaptic inhibition distorts the postsynaptic neuronal dynamics. If g_{inh} is greater than a *critical coupling*, g_{crit}^*,
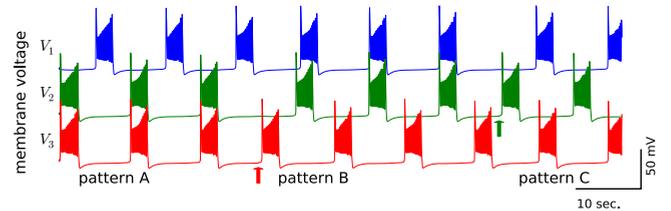
FIG. 2. (Color online) Stable polyrhythmic patterns in the NCM. Two 0.5-mV kicks (arrows) applied to membrane voltages $V_i(t)$ cause the NCM to switch among the three coexistent pacemaker patterns (A, B, and C). Parameters are $\sigma = 0$, $g = 20$ pS.
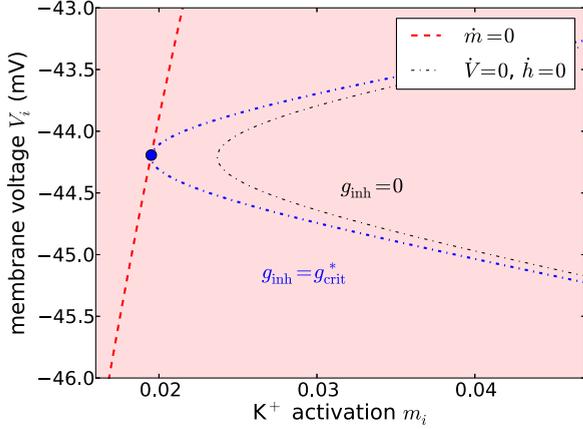
FIG. 3. (Color online) Critical synaptic strength in the neuronal burster. We show the shaded region of state space from Fig. 1 (lower-left corner there). Constant inhibition, at coupling strengths $g_{inh} > g_{crit}^*$, induces a saddle-node bifurcation by shifting the fast nullcline (dashed-dotted black lines) across the slow one [dashed (red) line]. The critical value g_{crit}^*, at which nullclines are tangent (filled circle), therefore separates a *soft* coupling from a *hard* coupling that can lock down the postsynaptic burster.

the presynaptic burst transiently stabilizes all postsynaptic neurons at a state within the quiescent phase. Unlike this *hard-lock* inhibition, a *soft-lock* inhibition at subcritical values ($g_{inh} < g_{crit}^*$) only slows the postsynaptic burst initiation.

The soft- to hard-lock transition occurs if inhibition is strong enough to give rise to a stable fixed point in the quiescent phase of postsynaptic bursting dynamics. Then the postsynaptic neuron is locked down in the quiescent state. Here, we treat g_{inh} as a bifurcation parameter. At $g_{inh} = g_{crit}^*$, a saddle-node bifurcation gives birth to a stable equilibrium, at which the postsynaptic neuron rests in the quiescent phase. In the state space, the bifurcation point is characterized by tangency of all *nullclines*, i.e., curves or surfaces at which time derivatives are 0 (cf. Fig. 3). The slow nullcline, $\dot{m}_i = 0$, is given by

$$m_i = m_{K_2}^\infty(V_i). \tag{5}$$

The fast nullcline, $(\dot{V}_i, \dot{h}_i) = 0$, is given by

$$h_i = h^\infty(V_i),$$
$$0 = -I_i^{Na} - I_i^{K_2} - I_i^L - \sum_{j \neq i} I_{ij}^{inh}. \tag{6}$$

We want to determine the g_{crit}^* at which one presynaptic burst can induce bifurcation in the postsynaptic dynamics. To test this, we set

$$\sum_{j \neq i} I_{ij}^{inh} = g_{inh}(V_i - E_{inh}). \tag{7}$$

In the following we drop the subscript i. The critical coupling strength g_{crit}^*, at which the slow [Eq. (5)] and fast [Eq. (6)] nullclines are tangent, is determined as a solution to the following equations implicit in V [we set $m = m_{K_2}^\infty(V)$ and

$h = h^\infty(V)$]:

$$0 = -I^{Na} - I^{K_2} - I^L - g_{crit}^*(V - E_{inh}),$$
$$0 = \frac{d}{dV}[-I^{Na} - I^{K_2} - I^L - g_{crit}^*(V - E_{inh})]. \tag{8}$$

This soft- to hard-lock transition leads to a qualitative change in network dynamics reflected in its rhythm robustness to small fluctuations. Below, we introduce such fluctuations and analyze their effect on the dynamics through Monte Carlo simulations.

In Sec. IV, we generalize the soft- to hard-lock transition to a generic bifurcation model. From the generalization we derive an approximation of g_{crit}^* that can be directly estimated from a voltage trace.

D. Mean free path description of noise-induced rhythm switching

Uncorrelated Gaussian white noise $I_i^{rand} = I_0 + \sigma\xi_i(t)$, with mean I_0, intensity σ^2, and $\langle\xi_i(t)\xi_j(t')\rangle = \delta(t - t')\delta_{ij}$, is used to study rhythm robustness to perturbations. Such noise may also emerge as the summated action of circuit-external synaptic projections [44]. Noise can dephase bursts at weak coupling and cause alternations from one bursting pattern to another. At strong coupling, this rhythm switching becomes frequent and unpredictable [Fig. 4(a)], even for weak noise.

To effectively analyze the statistics of switching, we cast the stochastic polyrhythmic dynamics of the NCM as a two-dimensional (2D) random walk. The three pacemaker patterns (Fig. 2) are mapped to three directions of motion in the physical
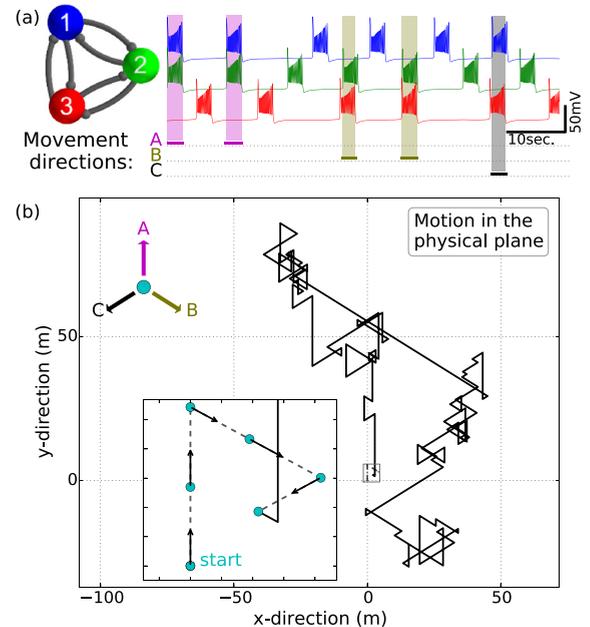
FIG. 4. (Color online) (a) NCM of three bursters (blue, 1; green, 2; red, 3) randomly switches among three pacemaker patterns in the voltage trace for coupling strength $g_{inh} = 15$ pS and noise $\sigma^2 = 0.0025$ pA^2/s. (b) Coincident bursts (shaded regions) are mapped into shifts in the A-B-C directions of 2D random walks. Inset: Random walk episode corresponding to the voltage trace in (a). The mean free path of the trajectory is 3.8 steps.

plane. Specifically, membrane voltages of NCM neurons are streamed into three burst-coincidence detectors—one for each pair of neurons—that, upon coincidence, activate a motion of an animat. A coincidence of bursts occurring in neurons 1 and 2 is assigned a shift with the velocity vector $(0,1)$. Coincident bursts in neurons 1 and 3 and in neurons 2 and 3 are assigned the vectors $(\sqrt{3}/2,-1/2)$ and $(-\sqrt{3}/2,-1/2)$, respectively [Fig. 4(b)].

Without noise, the animat moves in the direction set by the initial bursting pattern. At finite noise levels the NCM either repeats the same bursting pattern or switches to another pattern, which in turn changes the animat's directions (Fig. 4). We quantify the robustness of the NCM polyrhythms by the *mean free path* (MFP) of the animat's movement in response to noise. The MFP is defined as the average number of consecutive steps in a given direction. It is related to the transition probabilities of Markov chain approximations [7,45].

III. STRONG SYNAPTIC COUPLING DESTABILIZES POLYRHYTHMS

The synaptic coupling strength g_{inh} is the obvious parameter to control the robustness of NCM polyrhythms. We compute the MFP at a variety of coupling strengths and noise intensities, and we identify a nonmonotonous dependence of the MFP on g_{inh}, summarized in the biparametric sweep in Fig. 5. The key characteristics are that (i) the MFP reaches a maximum at an optimal coupling strength g_{opt}, which is in a vicinity of the soft- to hard-lock transition of network dynamics (at g_{crit}^*); and (ii) at sufficiently large g_{inh}, decreasing σ^2 does not lead to a noticeable increase in the MFP, which becomes smaller than two steps, thus indicating that bursting patterns alternate almost every cycle.

These findings are counterintuitive, because typically, increasing the coupling strength regularizes the dynamics of diffusively coupled oscillators and stabilizes the synchronized states against noise [46], although counter examples of dephasing coupled oscillators with increases in coupling
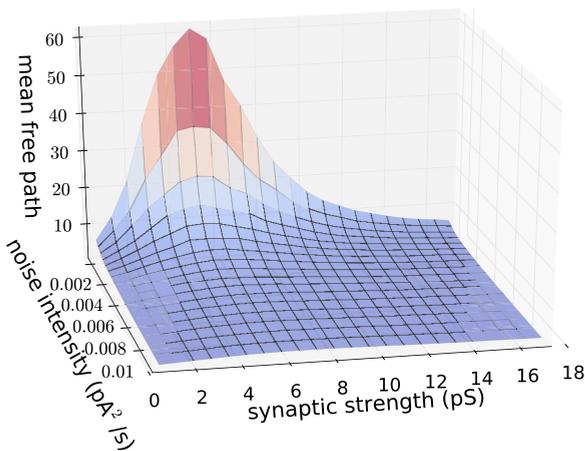
FIG. 5. (Color online) Nonmonotonous dependence of the mean free path (MFP) on the synaptic strength g_{inh}. For a plausible range of noise intensities, σ^2, the MFP reveals a synaptic strength of maximal robustness, $g_{\mathrm{opt}} \simeq 5.5$ pS, comparable with the critical coupling $g_{\mathrm{crit}} = 6.1$ pS [Eq. (10)].
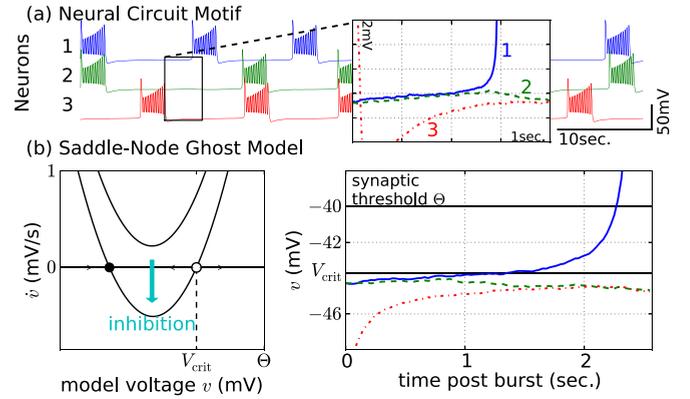
FIG. 6. (Color online) Hard-lock mechanism of rhythm switching. (a) A typical rhythm switching event (inlet) occurs upon noise-induced separation of neurons 1 and 2. Neuron 1 reaches Θ and inhibits neuron 2 from bursting. (b) The quiescent phase of postsynaptic neurons undergoes a saddle-node bifurcation upon activation of inhibition (left panel). The location of the unstable point marks the critical voltage V_{crit} [Eq. (11)] separating rhythm switching from coincident bursting: in the right panel, model neuron 2 [Eq. (9)] stays below V_{crit}, thus switching rhythms. Parameters: $g_{\mathrm{inh}} = 20$ pS, $\sigma^2 = 0.01$ pA^2/s, $V_0 = -44.3$ mV, $\varepsilon = 0.22$ mV/s, $\alpha = 1.53$ mV^{-1} s^{-1}.

strength are also known [47]. The value of g_{opt} at which the MFP is maximized corresponds to the highest degree of robustness of the network dynamics. At $g_{\mathrm{inh}} > g_{\mathrm{opt}}$, the NCM dynamics becomes increasingly vulnerable to noise, or other perturbations, and bursting pattern alternation intensifies due to the soft- to hard-lock transition, as we explain below. Our simulations indicate only a weak dependence of the optimal coupling strength on the noise intensity, which justifies our perturbation approach.

Vulnerable phase of the polyrhythms beyond the soft- to hard-lock transition

Beyond the soft- to hard-lock transition ($g_{\mathrm{inh}} > g_{\mathrm{crit}}^*$), rhythm switching is enhanced and occurs predominantly within a vulnerable phase of bursting patterns, as shown in the inset in Fig. 6(a). Here, simultaneous bursting of two neurons depends on whether both go together above a critical voltage V_{crit}. The vulnerable phase starts when neuron 3 finishes its burst discharge, and its voltage V_3 drops below the synaptic threshold Θ [Eq. (4)]. The consequent loss of synaptic inhibition releases the temporarily hard-locked neurons 1 and 2 [48]. Released, neurons 1 and 2 individually initiate their bursting cycles by raising the membrane voltages V_1 and V_2. While they are below Θ, they do not interact. In this phase, random perturbations drive the neurons apart, creating a small delay between V_1 and V_2. Neuron 1 reaches the threshold first. As V_1 passes Θ, neuron 1 starts to inhibit neuron 2. Because V_2 has not yet crossed V_{crit}, neuron 2 is held in hyperpolarized quiescence for the burst duration of neuron 1. Given that the burst is sufficiently long, postsynaptic neurons 2 and 3 remain in the locked state.

In contrast, the burst of neuron 1 is not followed by rhythm switching [Fig. 6(a)]: After the burst, neurons 2 and 3 start advancing towards the synaptic threshold. Now V_3

has surpassed V_{crit} as V_2, ahead of V_3, crosses Θ. Therefore, both neurons enter the bursting phase, leading to a temporal overlap of their bursts, and they complete a pacemaker pattern. These two scenarios explain the source of vulnerability of pacemaker patterns to perturbations beyond the soft- to hard-lock transition.

IV. SADDLE-NODE GHOST MODEL OF THE SOFT- TO HARD-LOCK TRANSITION

The soft- to hard-lock transition (Sec. II C) provides the mechanism that leads to the emergence of the vulnerable phase in the neuronal dynamics [Eq. (1)], as described in the previous section. Based on the bifurcation structure of neuronal dynamics, we devise a generic model that describes this vulnerable phase. The approach allows us to provide a link between critical voltage and critical synaptic strength. It also allows us to derive estimates V_{crit} and g_{crit} of these quantities from voltage traces only.

The neuronal dynamics at hard-lock coupling is characterized by a transient saddle-node bifurcation upon synaptic activation: the supercritical ($g_{\text{inh}} > g^*_{\text{crit}}$) synaptic inhibition ties the postsynaptic burster to the stable fixed point when the presynaptic burster is active (cf. Fig. 3). In the state-space vicinity of the bifurcation, the uncoupled neuronal dynamics is approximated by a quadratic normal form equation, $\dot{v} = \varepsilon + \alpha(v - V_0)^2$ [32]. The gap parameter, $0 < \varepsilon \ll 1$ mV/s, determines the speed at which the saddle-node" ghost" is passed. Adding noise and coupling, we derive the saddle-node ghost dynamics for model voltages v_i ($i = 1,2,3$):

$$\dot{v}_i = \varepsilon + \alpha(v_i - V_0)^2 - \left[\sigma \xi_i(t) + \sum_j I^{\text{inh}}_{ij}\right] C^{-1}. \quad (9)$$

Synaptic currents I^{inh}_{ij} and noise $\sigma \xi_i(t)$ are taken from the original NCM equation [Eq. (1)]. The parameters ε, α, and V_0 are estimated from the burster voltage trace $V(t)$ as described in Sec. IV A.

The saddle-node ghost model allows us to approximate the critical coupling g^*_{crit} by an estimate g_{crit}. It is the synaptic strength at which a single active synapse leads to the saddle-node bifurcation in the postsynaptic neuron (cf. Fig. 3). The situation is modeled by setting $\sigma = 0$ and $\sum_j I^{\text{inh}}_{ij} = g_{\text{inh}}(v_i - E_{\text{inh}})$ in Eq. (9): the saddle-node bifurcation occurs at

$$g_{\text{crit}} = 2C(\alpha(E_{\text{inh}} - V_0) + \sqrt{\alpha^2(E_{\text{inh}} - V_0)^2 + \varepsilon\alpha}). \quad (10)$$

For values $g_{\text{inh}} > g_{\text{crit}}$, a pair of fixed points emerges from the saddle-node bifurcation. The critical voltage V_{crit} is approximated by the position of the unstable fixed point:

$$V_{\text{crit}} = V_0 + \frac{g_{\text{inh}}}{2\alpha C} + \sqrt{\frac{g^2_{\text{inh}}}{4\alpha^2 C^2} - \frac{C\varepsilon + g_{\text{inh}}(E_{\text{inh}} - V_0)}{\alpha C}}. \quad (11)$$

Figure 6(b) illustrates the model dynamics of rhythm switching: v_1 surmounts the synaptic threshold Θ, whereas $v_2 < V_{\text{crit}}$ remains hard-locked within the basin of attraction of the transient stable state for $g_{\text{inh}} > g_{\text{crit}}$.

The correspondence of g^*_{crit} and g_{crit} is not perfect as discussed in the Appendix. However, the procedure for
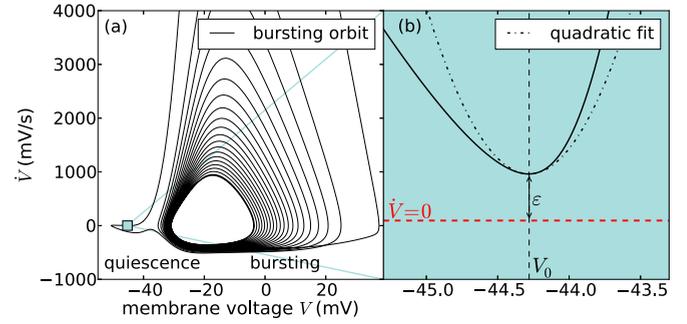
FIG. 7. (Color online) Estimation procedure of the saddle-node ghost equation. (a) Time derivative $\dot{V}$ on the periodic orbit shows a complicated dependence on V. (b) Locally, $\dot{V}$ can be expressed as a function, $F(V) = \dot{V}$. Parameters ε, V_0, and α of Eq. (9) are determined so that the quadratic fit (dash-dotted line) matches $F(V)$ (solid line) at the local minimum of the quiescent period. Ghost model parameters: $V_0 = -44.3$ mV, $\epsilon = 0.22$ mV/s, $\alpha = 1.53$ mV^{-1} s^{-1}.

obtaining g_{crit} is almost equation-free, as opposed to g^*_{crit}, for which the full Hodgkin-Huxley equations are needed. The estimate g_{crit} can thus also be obtained from empirical data. This highlights the benefits of the additional abstraction contained in the saddle-node ghost approach.

Estimation procedure of the saddle-node ghost model parameters

Parameters ε, α, and V_0 of the ghost model [Eq. (9)] are estimated from the voltage dynamics $V(t)$ of an uncoupled burster model [Eq. (1) at $g_{\text{inh}} = \sigma = 0$], as illustrated in Fig. 7. First, the periodic bursting orbit is obtained [solid line in Fig. 7(a)]. Within the quiescent phase of the bursting orbit, we express $\dot{V}$ as a function, $F(V)$ [solid line in Fig. 7(b)]. This is only possible locally. The function $F(V)$ yields a good representation of the saddle-node bifurcation, which appears if coupling is activated. However, we describe the transient saddle-node bifurcation on a higher level of abstraction by formulating the normal-form equation $\dot{v} = \varepsilon + \alpha(v - V_0)^2$ [cf. Eq. (9)]. Its parameters can be estimated directly from $F(V)$: at V_0, $F(V)$ is minimal, the minimum is $\varepsilon = F(V_0)$, and $2\alpha = F''(V_0)$. An example estimate is shown in Fig. 7(b).

The estimation procedure requires only traces of the uncoupled membrane voltage dynamics. In principle, it can also be applied to empirical data.

V. MODIFICATIONS FOR ROBUST POLYRHYTHMICITY

By taking into account the hard-lock switching mechanism, we can now balance the parameters to enhance the robustness of the NCM to noise. Foremost, we choose the optimal coupling strength (cf. Fig. 5). In addition, we present two strategies to enhance the robustness further: increasing the model parameter ε increases the ratio of drift and diffusion within the vulnerable phase after the quiescent neurons are released from inhibition [cf. Fig. 6(b)]. This gives the neurons a greater chance to enter the bursting phase simultaneously. Alternatively, the synaptic activation is made more gradual, which simply gives the two neurons more time to traverse the vulnerable phase before inhibition kicks in and separates the two neurons.
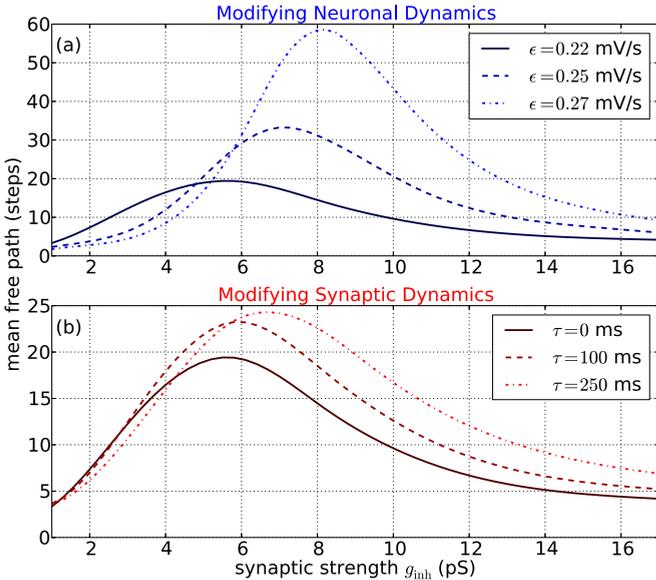
FIG. 8. (Color online) Improving the robustness of bursting polyrhythms. (a) MFP dependence on g_{inh} for $\varepsilon = 0.22$ mV/s at $V^{K_2} = 3$ mV, 0.25 mV/s at 3.5 mV, and 0.27 mV/s at 4 mV. The optimum, g_{opt}, shifts towards a higher g_{inh}. (b) MFP dependence on g_{inh} in the NCM with instantaneous $\tau = 0$ and delayed synapses $\tau = 100$ and 250 ms. Parameters: $V^{K_2} = 3$ mV, $\sigma^2 = 0.0025$ pA^2/s.

A. Neuronal modifications

Parameter ε approximates the smallest distance between slow and fast nullclines at $g_{inh} = 0$ (cf. Fig. 3). The complex Hodgkin-Huxley model allows for a variety of neuronal modifications that increase ε, all of which are aimed at altering the distance between nullclines.

In the particular model used in this study, an effective way to regulate the model parameter ε is to adjust the K$^+$ activation potential, V^{K_2} [Eq. (3)]: increasing V^{K_2} from 3 to 4 mV changes ε from 0.22 to 0.27 mV/s [49]. This change in neuronal dynamics enhances the MFP from 20 to 60 steps at g_{opt}, as shown in Fig. 8(a).

B. Synaptic modifications

Alongside the synaptic strength, the functional form of coupling can also be altered to enhance network robustness. We demonstrate that subtle synaptic modifications can alter robustness properties by making the onset of inhibition more gradual. For this, we slightly increase the synaptic time scale τ [Eq. (4)].

As shown in Fig. 8(b), $\tau = 250$ ms yields an optimal MFP of about 25 steps, as opposed to 20 steps at $\tau = 0$. Alternatively, one could also raise the synaptic threshold Θ, thus allowing more time for the systems to reach the bursting phase.

VI. CONCLUSIONS

Perturbation-induced switching between functional rhythms is a limiting factor to multifunctionality in neural networks. The assertion is supported by our analysis of the inhibitory NCM [Eq. (1)]: it demonstrates three coexisting bursting rhythms among which switching is frequently observed, indicating a high degree of vulnerability of polyrhythms. Switching among rhythms occurs within a vulnerable phase which is highly sensitive to perturbations. We uncover this phase by applying random perturbations to the NCM.

To recover rhythm robustness, we alter a variety of model parameters such as the synaptic strength, the principal parameter of synchrony. We find that strengthening synaptic coupling fulfills a dual role: at weak coupling the stability increases against gradual dephasing of bursting patterns [43,46,50], but at strong coupling the rhythm robustness decreases due to sensitization of the vulnerable phase. This duality is due to a coupling-dependent soft- to hard-lock transition. When strengthening coupling beyond the transition point, gradual dephasing of polyrhythms is further suppressed, but abrupt switching becomes more likely as well. Correspondingly, we find an optimal value of synaptic strength for which polyrhythms are maximally robust (cf. Fig. 5). This noise-induced rhythm switching is different from other mechanisms of coupling-induced dephasing [47,51,52], where noise does not play a key role. We note a similarity to Brownian motions in tilted periodic potentials where the diffusion coefficient becomes nonmonotonous and greatly amplified at a critical tilt [53,54].

We generalize our results by formulating the soft- to hard-lock transition in terms of a generic saddle-node bifurcation. This description has no reference to the number of oscillators in the network, or their biophysical interpretation. Therefore, the description generalizes the switching mechanism to a variety of oscillator networks. In larger inhibitory networks, the mechanism may also influence the distribution of cluster sizes in networks, where a large cluster can become vulnerable if its collective coupling exceeds an optimal strength dictated by the soft- to hard-lock transition. Applications may include memory processes [55], perceptual multistability [14,56], robotic locomotion [57], and generic phase oscillator networks [17]. The mechanism may be equally observable in metastable systems, yielding an alternative description of neural code [58].

Using the mechanism-based selection of neuronal parameters, we achieve a threefold enhancement of rhythm robustness (Fig. 8). The enhancement is achieved without optimizing a multitude of parameters in our NCM model, which would be a costly task *in silico*. Foremost, such high-dimensional optimization is unfeasible in synthetic-neurobiological experiments, in which simultaneous control of multiple biological parameters is complicated [59]. Our analysis highlights the strengths of biodynamical modeling to control biological systems and to avoid pitfalls emerging at the intersection of noise and nonlinearity.

TABLE I. Typical parameter values used in this work.

Parameter	Description	Value
C	Membrane capacitance	0.5 nF
g_{Na}	Na$^+$ conductance	160 nS
g_{K_2}	K$^+$ conductance	30 nS
g_L	Leakage conductance	8 nS
E_{Na}	Na$^+$ resting potential	45 mV
E_K	K$^+$ resting potential	-70 mV
E_L	Leak resting potential	-46 mV
τ_{Na}	Na$^+$ time scale	0.0405 s
τ_{K_2}	K$^+$ time scale	0.9 s
V^{Na}	Na$^+$ activation threshold	-30.5 mV
V^h	Na$^+$ inactivation threshold	-32.5 mV
V^{K_2}	K$^+$ activation threshold	3 mV
s^{Na}	Na$^+$ activation slope	0.15 mV^{-1}
s^h	Na$^+$ inactivation slope	-0.5 mV^{-1}
s^{K_2}	K$^+$ activation slope	0.083 mV^{-1}
E_{inh}	Synaptic resting potential	-62.5 mV
λ	Synaptic activation slope	1 mV^{-1}
Θ	Synaptic threshold	-40 mV
I_0	Synaptic noise mean	6 pA
σ^2	Noise intensity	0.0025 pA^2/s

University of Nizhni Novgorod, the agreement of August 27, 2013.

APPENDIX

1. Full NCM model equations

For each of the three neurons, $i = 1, 2, 3$, the membrane voltages dynamics $V_i(t)$ is modeled by Hodgkin-Huxley-type equations:

$$C\dot{V}_i = -I_i^{Na} - I_i^{K_2} - I_i^{L} - I_i^{rand} - \sum_{j \neq i} I_{ij}^{inh},$$

$$I_i^L = g_L(V_i - E_L), \quad I_i^{K_2} = g_{K_2} m_i^2 (V_i - E_K),$$

$$I_i^{Na} = g_{Na} m_{Na}^3 h_i (V_i - E_{Na}), \quad m_{Na} = m_{Na}^\infty(V_i),$$

$$\tau_{Na} \dot{h}_i = h^\infty(V_i) - h_i, \quad \tau_{K_2} \dot{m}_i = m_{K_2}^\infty(V_i) - m_i,$$

$$h^\infty(V) = (1 + \exp(-s^h(V - V^h)))^{-1}, \quad \text{(A1)}$$

$$m_{Na}^\infty(V) = (1 + \exp(-s^{Na}(V - V^{Na})))^{-1},$$

$$m_{K_2}^\infty(V) = (1 + \exp(-s^{K_2}(V - V^{K_2})))^{-1},$$

$$I_{ij}^{inh} = g_{inh}(V_i - E_{inh})/[1 + \exp(-\lambda(\Theta - V_j))],$$

$$I^{rand} = I_0 + \sigma \xi_i(t), \quad \langle \xi_i(t)\xi_j(t')\rangle = \delta_{ij}\delta(t - t').$$

Table I lists all free parameter values used in this work.

We approximate the solution to this stochastic differential equation with the Euler-Maruyama method with a fixed time step width of $\Delta t = 0.001$ s. This value yields about 180 points
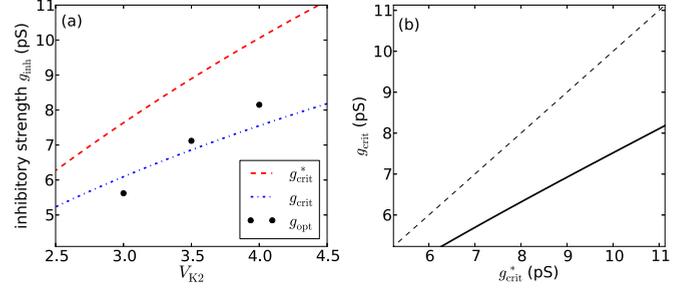
FIG. 9. (Color online) Comparison of critical and optimal inhibitory strength. (a) For different values of V^{K_2}, g_{crit} [dashed-dotted (blue) line] and g_{crit}^* [dashed (red) line] approximate the optimal coupling g_{opt} (circles) reasonably well. (b) The ghost model approximation g_{crit} systematically underestimates the bifurcation value g_{crit}^*, seen as deviations from the diagonal (dashed black line). Parameter: $\sigma^2 = 0.0025$ pA^2/s.

per oscillation in the fast spiking dynamics. We tested other values of Δt to confirm the numerical stability of our results.

A PYTHON code that simulates the stochastic network motif for these parameter values is included in the Supplemental Material for convenience [60].

2. Relation of critical and optimal coupling

We compare the soft- to hard-lock transition value g_{crit}^* from Eq. (8) to its estimate g_{crit} from the saddle-node ghost model [Eq. (9)] and to the optimal coupling strength g_{opt} from the full stochastic network, all at a range of values of the parameter V^{K_2} [Fig. 8(a)].

The close proximity of all three quantities underlines the relevance of the soft- to hard-lock transition to rhythm robustness [Fig. 9(a)]: both g_{crit}^* and g_{crit} predict the optimal value of the inhibitory strength, g_{opt}, beyond which the network rapidly loses robustness. Notably, the real bifurcation value g_{crit}^* overestimates g_{opt}. This is expected because a stochastic dynamics typically anticipates a transition, e.g., bifurcation, in its corresponding deterministic dynamics. Critical coupling g_{crit} of the ghost model yields a better predictor to g_{opt} than g_{crit}^*. Notice, however, that g_{crit} was only designed as a more general quantity that closely tracks g_{crit}^*.

We find that g_{crit} systematically underestimates g_{crit}^* and that the better prediction of g_{opt} is thus somewhat "accidental.' Let us outline the origin of this systematic error of g_{crit} in approximating g_{crit}^*. As shown in Fig. 3(b), increasing g_{inh} moves the fast nullcline approximately horizontally (in the m_{K_2} direction) towards the slow nullcline. This direction does not follow the shortest distance between the two nullclines. The ghost model, on the other hand, approximates this shortest distance with the parameter ε and assumes that g_{inh} yields shift in that very direction. In consequence, smaller values of g_{inh} induce a transition in the ghost model approximation. Note that the skewed geometry is also visible in Fig. 7, where a small rotation of axes would allow for a better quadratic fit.

[1] S. Buldyrev, R. Parshani, G. Paul, H. Stanley, and S. Havlin, Nature **464**, 1025 (2010).

[2] R. K. Pradhan and V. S. Chakravarthy, Acta Physiol. **201**, 193 (2011).

[3] C. M. Schneider, A. A. Moreira, J. S. Andrade, S. Havlin, and H. J. Herrmann, Proc. Natl. Acad. Sci. USA **108**, 3838 (2011).

[4] A. Bashan, R. P. Bartsch, J. W. Kantelhardt, S. Havlin, and P. C. Ivanov, Nat. Commun. **3**, 702 (2012).

[5] A. N. Pisarchik and U. Feudel, Phys. Rep. **540**, 167 (2014).

[6] M. Thattai and A. Oudenaarden, Proc. Natl. Acad. Sci. USA **98**, 8614 (2001).

[7] C. Gupta, J. M. López, W. Ott, K. Josić, and M. R. Bennett, Phys. Rev. Lett. **111**, 058104 (2013).

[8] R. E. Hoffman, D. M. Quinlan, C. M. Mazure, and M. T. M., Biol. Psychiatry **49**, 500 (2001).

[9] E. Ermentrout and N. Kopell, Proc. Natl. Acad. Sci. USA **101**, 15482 (2004).

[10] A. A. Prinz, Curr. Opin. Neurobiol. **16**, 615 (2006).

[11] J. J. Bouyer, M. F. Montaron, J. M. Vahne, M. P. Albert, and A. Rougeul, Neuroscience **22**, 863 (1987).

[12] C. M. Gray and W. Singer, Proc. Natl. Acad. Sci. USA **86**, 1698 (1989).

[13] S. Cheng and L. M. Frank, Neuron **57**, 303 (2008).

[14] D. Golomb and J. Rinzel, Physica D: Nonlin. Phenom. **72**, 259 (1994).

[15] J. Rubin and D. Terman, J. Math. Biol. **41**, 513 (2000).

[16] D. T. W. Chik, S. Coombes, and Z. D. Wang, Phys. Rev. E **70**, 011908 (2004).

[17] M. Komarov and A. Pikovsky, Phys. Rev. Lett. **111**, 204101 (2013).

[18] A. Engel and W. Singer, Trends Cognit. Sci. **5**, 16 (2001).

[19] C. Gilbert and W. Li, Nat. Rev. Neurosci. **14**, 350 (2013).

[20] J. Keeler, E. Pichler, and J. Ross, Proc. Natl. Acad. Sci. USA **86**, 1712 (1989).

[21] D. Breuer, M. Timme, and R.-M. Memmesheimer, BMC Neurosci. **14**, 273 (2013).

[22] P. Miller, J. Math. Neurosci. **3**, 19 (2013).

[23] A. M. Thomson, D. C. West, Y. Wang, and A. P. Bannister, Cerebral Cortex **12**, 936 (2002).

[24] R. Milo, S. Shen-Orr, S. Itzkovitz, N. Kashtan, D. Chklovskii, and U. Alon, Science **298**, 824 (2002).

[25] O. Sporns and R. Kötter, PLoS Biol. **2**, e369 (2004).

[26] S. Song, P. J. Sjöström, M. Reigl, S. Nelson, and D. B. Chklovskii, PLoS Biol. **3**, e68 (2005).

[27] R. Perin, T. K. Berger, and H. Markram, Proc. Natl. Acad. Sci. USA **108**, 5419 (2011).

[28] J. Qian, A. Hintze, and C. Adami, PLoS ONE **6**, e17013 (2011).

[29] F. S. Matias, P. V. Carelli, C. R. Mirasso, and M. Copelli, Phys. Rev. E **84**, 021922 (2011).

[30] E. Marder and R. L. Calabrese, Physiol. Rev. **76**, 687 (1996).

[31] S. Coombes and P. Bressloff, *Bursting: The Genesis of Rhythm in the Nervous System* (World Scientific, Singapore, 2005).

[32] E. M. Izhikevich, *Dynamical Systems in Neuroscience* (MIT Press, Cambridge, MA, 2007).

[33] A. Shilnikov, R. Gordon, and I. Belykh, Chaos **18**, 037120 (2008).

[34] C. Vreeswijk, L. Abbott, and G. Bard Ermentrout, J. Comput. Neurosci. **1**, 313 (1994).

[35] S. Jalil, I. Belykh, and A. Shilnikov, Phys. Rev. E **85**, 036214 (2012).

[36] P. Channell, I. Fuwape, A. Neiman, and A. Shilnikov, J. Comput. Neurosci. **27**, 527 (2009).

[37] B. Lindner, J. Garca-Ojalvo, A. Neiman, and L. Schimansky-Geier, Phys. Rep. **392**, 321 (2004).

[38] H. Braun, J. Schwabedal, M. Dewald, C. Finke, S. Postnova, B. Huber, M.T. Wollweber, H. Schneider, M. Hirsch, K. Voigt, U. Feudel, and F. Moss, Chaos **21**, 047509 (2011).

[39] A. Shilnikov and G. Cymbalyuk, Phys. Rev. Lett. **94**, 048101 (2005).

[40] A. Shilnikov, Nonlin. Dynam. **68**, 305 (2012).

[41] J. Wojcik and A. Shilnikov, Physica D: Nonlin. Phenom. **240**, 1164 (2011).

[42] D. Somers and N. Kopell, Biol. Cybern. **68**, 393 (1993).

[43] J. Wojcik, R. Clewley, and A. Shilnikov, Phys. Rev. E **83**, 056209 (2011).

[44] J. L. Dideriksen, F. Negro, R. M. Enoka, and D. Farina, J. Neurophysiol. **107**, 3357 (2012).

[45] P. Hänggi, P. Talkner, and M. Borkovec, Rev. Mod. Phys. **62**, 251 (1990).

[46] A. Pikovsky, M. Rosenblum, and J. Kurths, *Synchronization. A Universal Concept in Nonlinear Sciences* (Cambridge University Press, Cambridge, 2001).

[47] S. K. Han, C. Kurrer, and Y. Kuramoto, Phys. Rev. Lett. **75**, 3190 (1995).

[48] I. Belykh, S. Jalil, and A. Shilnikov, Regul. Chaotic Dynam. **15**, 146 (2010).

[49] The single-cell quiescent interval also increases by 10%.

[50] J. Wojcik, J. Schwabedal, R. Clewley, and A. L. Shilnikov, PLoS ONE **9**, e92918 (2014).

[51] M. Rosenblum and A. Pikovsky, Phys. Rev. Lett. **98**, 064101 (2007).

[52] S. Ehrich, A. Pikovsky, and M. Rosenblum, Eur. Phys. J. Special Topics **222**, 2407 (2013).

[53] P. Reimann, C. Van den Broeck, H. Linke, P. Hänggi, J. M. Rubi, and A. Pérez-Madrid, Phys. Rev. Lett. **87**, 010602 (2001).

[54] D. Reguera, P. Reimann, P. Hänggi, and J. M. Rubi, Europhys. Lett. **57**, 644 (2002).

[55] X.-J. Wang and G. Buzsaki, J. Neurosci. **16**, 6402 (1996).

[56] A. Shpiro, R. Curtu, J. Rinzel, and N. Rubin, J. Neurophysiol. **97**, 462 (2007).

[57] G. Haynes, A. Rizzi, and D. Koditschek, Int. J. Robot. Res. **31**, 1712 (2012).

[58] M. I. Rabinovich, P. Varona, I. Tristan, and V. S. Afraimovich, Front. Comput. Neurosci. **8**, 22 (2014).

[59] C. J. Magnus, P. H. Lee, D. Atasoy, H. H. Su, L. L. Looger, and S. M. Sternson, Science **333**, 1292 (2011).

[60] See Supplemental Material at http://link.aps.org/supplemental/10.1103/PhysRevE.90.022715 for details on the PYTHON code. The PYTHON code is freely available at https://github.com/jusjusjus/StochasticNeuralMotif_PRE2014